© 2021. Published by The Company of Biologists Ltd | Journal of Cell Science (2022) 135, jcs252353. doi:10.1242/jcs.252353

REVIEW

SPECIAL ISSUE: CELL BIOLOGY OF LIPIDS

Dissecting lipid droplet biology with coherent Raman scattering microscopy

Tao Chen[1,*], Ahmet Yavuz[1,*] and Meng C. Wang[1,2,3,‡]

ABSTRACT

Lipid droplets (LDs) are lipid-rich organelles universally found in most cells. They serve as a key energy reservoir, actively participate in signal transduction and dynamically communicate with other organelles. LD dysfunction has been associated with a variety of diseases. The content level, composition and mobility of LDs are crucial for their physiological and pathological functions, and these different parameters of LDs are subject to regulation by genetic factors and environmental inputs. Coherent Raman scattering (CRS) microscopy utilizes optical nonlinear processes to probe the intrinsic chemical bond vibration, offering label-free, quantitative imaging of lipids *in vivo* with high chemical specificity and spatiotemporal resolution. In this Review, we provide an overview over the principle of CRS microscopy and its application in tracking different parameters of LDs in live cells and organisms. We also discuss the use of CRS microscopy in genetic screens to discover lipid regulatory mechanisms and in understanding disease-related lipid pathology.

KEY WORDS: Label-free imaging, Coherent Raman scattering microscopy, Lipid droplet, Lipid metabolism, Genetic screens

Introduction

Lipid droplets (LDs) are cellular organelles that are highly specialized; they contain a hydrophobic core of neutral lipids, triacylglycerol and/or sterol ester, enclosed by a single-layer membrane composed of phospholipids (Thiam and Ikonen, 2021) (Fig. 1A). LDs are vital hubs of cellular metabolism, as they are not only important for lipid storage, but also take part in the regulation of lipid synthesis, incorporation and breakdown, as well as lipid signaling (Bustos and Partridge, 2017; Jarc and Petan, 2020). Owing to the hydrophobic nature of the lipid core, LD-associated proteins predominantly anchor to the phospholipid membrane (Thiam and Dugail, 2019; Zhang and Liu, 2019). These proteins are crucial for the maintenance of the morphology and functionality of LDs, and they regulate lipid incorporation and lipolysis at LDs; they also mediate the interaction of LDs with other organelles and contribute to lipid signaling (Cui and Liu, 2020; Herker et al., 2021; Zhang and Liu, 2019). The current model of LD formation suggests that free fatty acids are firstly esterified and accumulate within the intermonolayer leaflets of endoplasmic reticulum (ER) to form lipid lenses, which further grow and then bud off from the ER to become droplets in the cytosol (Olzmann and Carvalho, 2019). These newly released small droplets can expand to large droplets through incorporation of more neutral lipids and coalescence with each other (Fig. 1A). The turnover of LDs is closely correlated with metabolic status. In lipolysis, lipids are hydrolyzed to release free fatty acids that can be utilized in mitochondrial and peroxisomal β-oxidation to generate energy, in phospholipid biogenesis as building blocks and in signal transduction as lipid messengers (Lass et al., 2011; Walther and Farese, 2012). With the mobilization of the lipid core, LDs reduce their size, decrease contacts with other organelles and the excess proteins on the surface are degraded (Lass et al., 2011; Olzmann and Carvalho, 2019; Thiam and Dugail, 2019). In recent years, there has been recognition that the roles of LDs greatly extend beyond them just being inert lipid reservoirs, and we now know they are an active platform for organelle crosstalk and cellular signaling (Gao and Goodman, 2015) (Fig. 1A). LD homeostasis is vital for organism health, and its disruption leads to a variety of metabolic diseases, such as obesity, hepatic steatosis and lipoatrophy (Walther and Farese, 2012). Importantly, the functionality of LDs is tightly linked with their size, composition and spatiotemporal distribution within the cell and organism. Methods to quantitatively analyze these different LD parameters at high spatial resolution in a physiologically relevant condition are crucial for understanding the regulation of LDs and their contribution to health and diseases.

Traditional biochemical approaches, including chromatography and mass spectrometry, have been applied to LDs extracted from cells, tissues or whole organisms. These quantitative analyses have been employed to profile the composition of neutral lipids in the core and phospholipids in the membrane of the extracted LDs (Ding et al., 2013). However, these approaches lose spatial information regarding LD distribution and heterogeneity. Furthermore, transmission electron microscopy has been exploited to image LDs *in situ*, and its ultrahigh resolution has successfully revealed nascent LDs as small as 50 nm (Ohsaki et al., 2014; Wang et al., 2016). Despite the ultrahigh resolution, identification of LDs smaller than 50 nm is not trivial, because they can be easily confused with other small cellular structures, such as endocytic vesicles. Imaging mass spectrometry can map the spatial distribution of a large number of lipid species, but the resolution is far less than what is needed for LDs, and it cannot probe samples under physiological conditions (Djambazova et al., 2020). Fluorescence microscopy is powerful for LD visualization *in vivo* through coupling with lipophilic fluorescent dyes and/or fluorescent fusions of LD-associated proteins (Brasaemle et al., 1997; Fam et al., 2018; Kuerschner et al., 2005, 2008; Listenberger and Brown, 2007). In addition, label-free imaging approaches, which require no exogenous molecules for labeling, further advance LD imaging at the most physiological conditions. Third-harmonic generation utilizes the third-order susceptibility inhomogeneity within the excitation volume to probe LDs (Débarre et al., 2006). Quantitative phase imaging (QPI) makes use of the refractive index to reconstruct cellular components contours. Optical diffraction tomography, a technology based on the principle of QPI, provides fast non-invasive imaging of cellular LDs in three dimensions (Kim

[1]Huffington Center on Aging, Baylor College of Medicine, Houston, TX 77030, USA. [2]Department of Molecular and Human Genetics, Baylor College of Medicine, Houston, TX 77030, USA. [3]Howard Hughes Medical Institute, Baylor College of Medicine, Houston, TX 77030, USA.
*These authors contributed equally to this work

‡Author for correspondence (wmeng@bcm.edu)

M.C.W., 0000-0002-5898-6007

Journal of Cell Science (2022) 135, jcs252353. doi:10.1242/jcs.252353

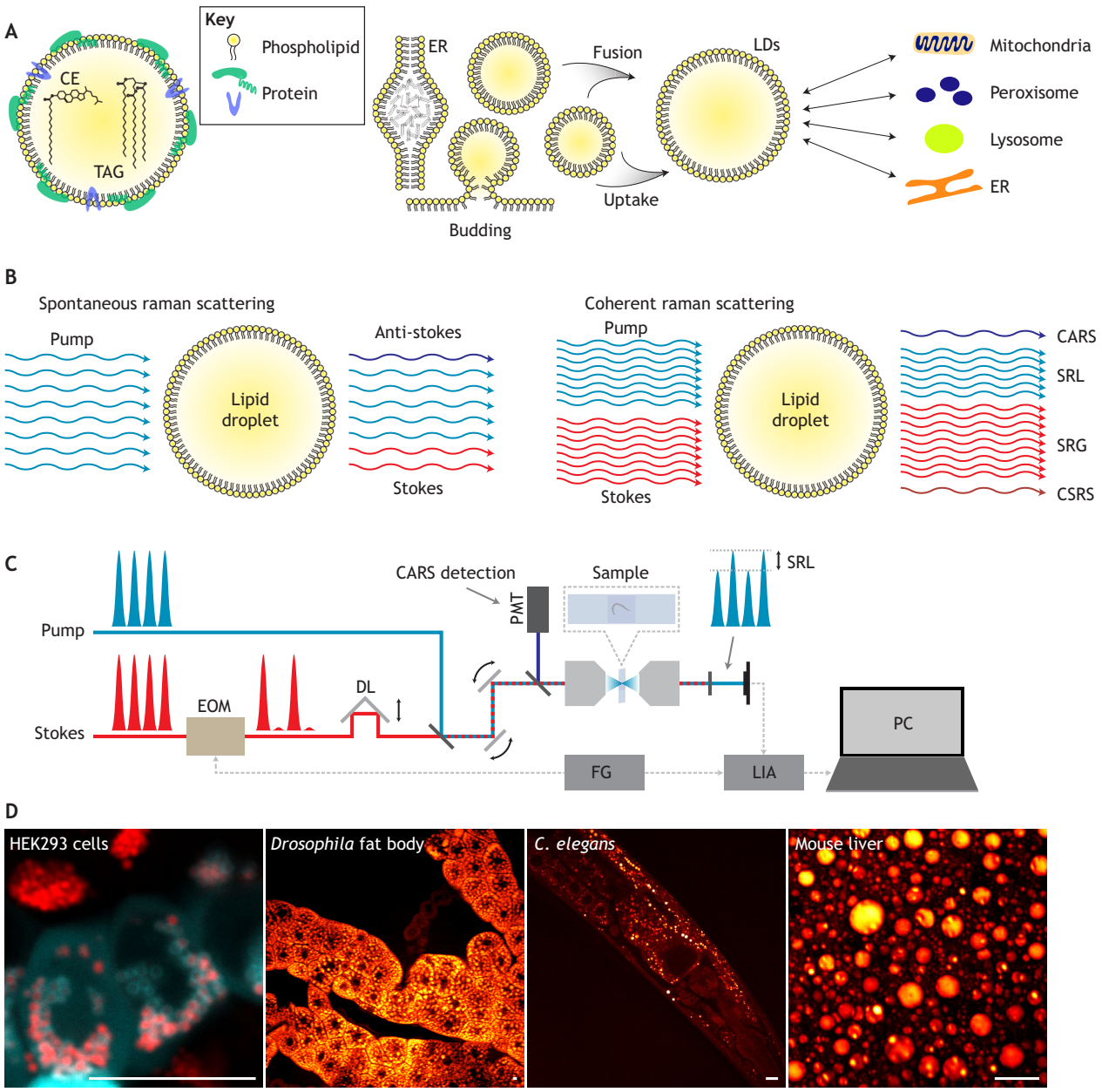

Fig. 1. Coherent Raman scattering microscopic imaging of LDs. (A) Lipid droplets (LDs) store cholesterol ester (CE) and triacylglycerol (TAG) in the core, which is enclosed by a single layer of phospholipid membrane into which various proteins are anchored. The formation of LDs starts with fatty acid esterification and accumulation in the endoplasmic reticulum (ER). Upon budding off from the ER, small LDs form larger ones through lipid incorporation and protein recruitment and/or coalescing with each other. LDs undergo dynamic interactions with other organelles. (B) Principle of spontaneous Raman and coherent Raman scattering. In spontaneous Raman scattering (SRS), a small fraction of pump photons will be converted to photons with increased energy (anti-Stokes photons) or decreased energy (Stokes photons). In coherent Raman scattering (CRS), the synchronized pump and Stokes photons can generate enhanced anti-Stokes fluorescence and transfer energy between each other mediated by the molecules. CARS, coherent anti-Stokes Raman scattering; SRL, stimulated Raman loss; SRG, stimulated Raman gain, CSRS, coherent Stokes Raman scattering. (C) An example of instrumentation for coherent Raman scattering microscopes. Synchronized and overlapped pump and Stokes lasers are directed into a laser scanning microscope. The intensity of the Stokes laser is modulated by an electro-opto modulator (EOM). The combined beam is focused on the sample, and the reflected anti-Stokes signal is collected and detected by a photo-mulitplier tube (PMT). The transmitted lasers are filtered; only the pump beam will transmit and reach the photodiode. The photo-electric current is sent to a lock-in amplifier (LIA) for demodulation and signal amplification. DL, delay line; FG, function generator. (D) Representative SRS images of LDs in various samples. From the left to the right are: cultured HEK293 cells (red for SRS and cyan for YFP labeled LSDP5) (Wang et al., 2011), fat body of *D. melanogaster* (Yu et al., 2014), *C. elegans*, and mice liver tissue section (Yu et al., 2014). Scale bar: 10 µm for all images. Images are adopted with permission from references.

et al., 2016). However, despite their advantage in tracking LDs *in vivo* with high spatial resolution, these imaging methods are often non- or semi-quantitative and lack chemical specificity to reveal LDs with different lipid composition.

Vibrational spectroscopic approaches, including infrared (IR) and Raman scattering, acquire contrast by probing the energy exchange between incident photons and the vibration of the chemical bonds. Through targeting LDs by the spectral signature of the abundant

aliphatic hydrocarbon in fatty acids, vibrational spectroscopy and microscopy offer imaging methods to identify LDs with chemical specificity. Compared with IR, which is based on absorption, Raman scattering is intrinsically free from large positive background signals, and it has less requirement on excitation wavelength, permitting higher spatial resolution with shorter excitation wavelengths in mapping (Jones et al., 2019). However, Raman scattering suffers from low signal intensity, therefore requiring long acquisition time, which limits its application in imaging live samples. Through coherent excitation and nonlinear processing, coherent Raman scattering (CRS) microscopy is able to enhance the Raman-scattering signal by several orders of magnitudes, enabling label-free fast imaging of LDs with high spatiotemporal resolution and chemical specificity (Cheng and Xie, 2015; Yu et al., 2014). In this Review, we will focus on CRS microscopy and introduce the principle behind its use to image LDs. We will also provide an overview of its recent biological applications in the discovery of new regulatory mechanisms of LDs and medical applications to understand disease pathology.

Principle of Raman scattering and coherent Raman scattering

CRS microscopy utilizes the same signal as spontaneous Raman scattering, which originates from the interaction between photons and chemical bond vibrations. In spontaneous Raman scattering, the vibrational energy of molecules, the energy acquired from relative motion between atomic nuclei, can be exchanged with incident photons. Consequently, a small fraction of photons undergoes frequency shifts after the energy exchange with a chemical bond. The frequency that is shifted towards the lower-energy end of the spectra is called the Stokes Raman scattering, and the frequency shifted towards the higher-energy end of the spectra is called the anti-Stokes Raman scattering (Camp and Cicerone, 2015; Zumbusch et al., 2013) (Fig. 1B). Correspondingly, the vibrational energy level of the chemical bond transits from the ground state to the excited state in the Stokes Raman scattering or vice versa in the anti-Stokes Raman scattering. The energy gain or loss of the photon equals the energy difference between the two vibrational states of the chemical bond, which is called the Raman shift. Since the Raman shift is a characteristic feature of a chemical bond, the detection of these frequency-shifted photons will reveal the presence of a specific chemical bond in a molecule. A spectrum of these frequency-shifted photons from Raman scattering, which is called the Raman spectrum, provides information on the composition and structure of chemical groups in a sample without any labeling. However, microscopic detection based on spontaneous Raman scattering experiences a natural drawback, in that the chance of a scattering event to happen in a Raman process (Nagli et al., 2008; Tian et al., 2007) is more than ten orders of magnitude lower than that of a fluorescence event (Lincoln et al., 2012), therefore, limiting the practical use of Raman scattering for live imaging.

Coherent excitation overcomes the limitation of spontaneous Raman scattering and enhances the signal up to eight orders of magnitude in a focused excitation volume, therefore making it sufficient for real-time imaging (Evans and Xie, 2008; Min et al., 2011). Coherent excitation requires incident lights of two different wavelengths, λ_p (the pump light) and λ_S (the Stokes light). When the frequency difference between the pump light (λ_p) and the Stokes light (λ_S) equals the vibrational energy of a chemical bond, the beating frequency will excite the chemical bonds to vibrate in a coordinated manner. The coherently excited molecules will carry out two types of processes amid nonlinear interaction with the light. The first type is the parametric process, in which lights of new wavelengths are generated but no photonic energy is transferred to the molecules. It includes the generations of anti-Stokes photons in coherent anti-Stokes Raman scattering (CARS) and Stokes photons in coherent Stokes Raman scattering (CSRS). They are the results of scattering of pump or Stokes photons by the coherently excited molecules. CARS is the dominant mechanism of the parametric process adopted in CRS microscopy. The second type is the dissipative process, in which no new wavelengths of lights are generated but a share of photonic energy is transferred to the molecules. In the dissipative process, the intensity of the pump light (λ_p) and Stokes lights (λ_S) will change in stimulated Raman scattering (SRS) (Woodbury and Ng, 1962) due to the energy conversion from the pump photon to the Stokes photon coupled with the coherent excitation of chemical bonds. In SRS, the pump and Stoke light experiences a power loss and gain, called stimulated Raman loss (SRL) and stimulated Raman gain (SRG), respectively. SRL is mostly adopted in the home-built SRS microscope. All of the above processes happen simultaneously upon resonance when the frequency difference between the pump and Stokes photons meets the vibrational energy of specific chemical bonds. Thus, both CARS and SRS signals can be used to probe molecules based on their chemical specificity, but there are important differences between them. First, CARS and SRS suffer from different backgrounds. In CARS, a non-resonant background is the major contamination to the true signal. The non-resonant background originates from nonlinear electronic responses to excitation lights, therefore presenting regardless of the frequency difference between the pump and Stokes lights. The non-resonant background can distort the Raman spectrum of the target. Various methods have been developed to eliminate the non-resonant background (Ganikhanov et al., 2006; Pope et al., 2013; Bradley et al., 2016; Masia et al., 2013). SRS is frequently hindered by a background originating from other nonlinear optical processes, which can be removed using polarization encoding (Hill et al., 2019). In general, SRS obtains a spectrum of the sample that is identical to its spontaneous Raman spectrum, offering a simple straightforward way of quantification, whereas in CARS, the non-resonant background can distort the spectrum and complicate the quantification process. However, with the effective removal of the non-resonant background using well-designed algorithms, the recovered Raman spectra offer a quantification capability comparable to SRS (Bradley et al., 2016; Masia et al., 2013). Secondly, CARS and SRS signals show different dependence on local molecule concentration. Ideally, CARS has a quadratic dependence on molecule concentration (Evans and Xie, 2008); however, the actual quantitative relationship can be shifted to in between linear and quadratic due to the non-resonant background. SRS, in contrast, presents a linear relationship between signal intensity and molecule concentration (Freudiger et al., 2008) (Fig. 2B). As two most commonly used approaches in CRS microscopy, the basis of CARS and SRS microscopes will be explained in the next section.

Basis of CARS and SRS microscopes

With decades of development, numerous configurations of CRS microscopes have been developed. A couple of excellent reviews (Zhang and Cheng, 2018; Zumbusch et al., 2013) have covered these different schemes. Here, we give an example and discuss several major considerations related to the example, including the use of an ultrafast laser system for excitation, a scanning microscope for image acquisition and a series of electronic devices for signal retrieval (Fig. 1C). An ultrafast laser system that can provide two excitation wavelengths is usually utilized, specifically with one tunable beam. As a critical step to obtain

Journal of Cell Science (2022) 135, jcs252353. doi:10.1242/jcs.252353

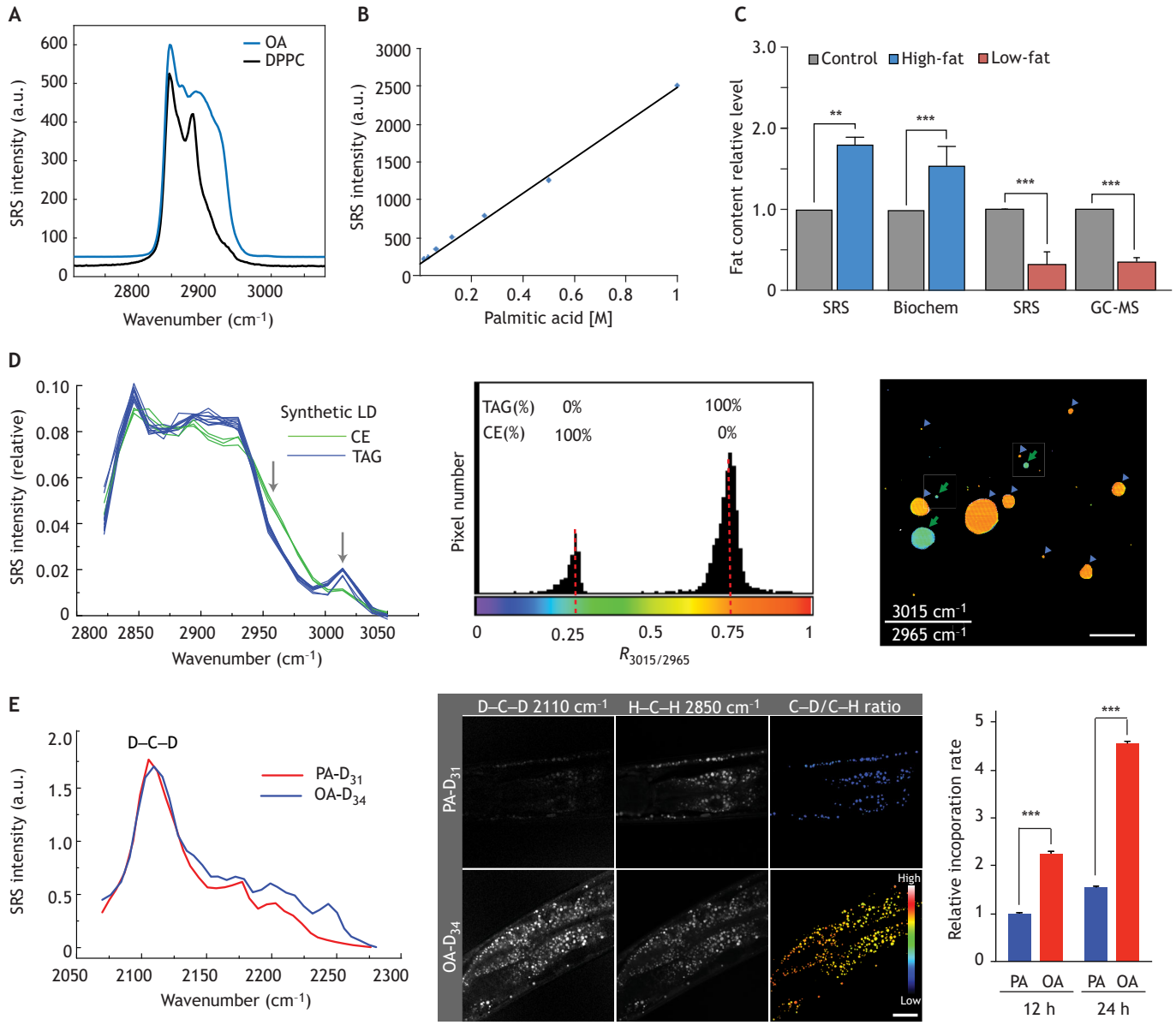

Fig. 2. SRS imaging of different LD parameters. (A) Representative SRS spectrum of dipalmitoylphosphatidylcholine (DPPC), a compound used to represent saturated lipid in research, and oleic acid (OA), showing the aliphatic hydrocarbon peak at 2845 cm^{-1}. (B) The standard curve of palmitic acid concentrations in DMSO solution demonstrates a linear concentration dependence (Yu et al., 2014). (C) Quantification of fat content levels using SRS, colorimetric biochemical assay (Biochem) and gas chromatography–mass spectrometry (GC-MS) analysis, yielding comparable results. Data from Mutlu et al. (2020) and Wang et al. (2011), and are shown as mean±s.d. (n=5–20 worms for SRS, n=15,000 worms for biochemistry and GC-MS). **P<0.01, ***P<0.001 (one-way ANOVA). (D) Application of SRS hyperspectral imaging to distinguish LDs containing cholesterol ester versus triacylglycerol. Left, SRS hyperspectra of individual synthetic LDs containing cholesterol ester or triacylglycerol showing visible differences at 3015 cm^{-1} and 2965 cm^{-1} (indicated by arrows) and how they are separated into two groups. Middle, the histogram of the signal ratio for each pixel between images at 3015 cm^{-1} and 2965 cm^{-1} ($R_{3015/2965}$) showing two peaks that correspond to either 100% of cholesterol ester or triacylglycerol. Right, image showing individual synthetic LDs containing either cholesterol ester (green arrows) or triacylglycerol (blue arrowheads). Scale bar: 20 µm. (E) Use of deuterated fatty acids to assess lipid dynamics. Left, SRS hyperspectra of deuterated palmitic acid ($PA\text{-}D_{31}$) and oleic acid ($OA\text{-}D_{34}$) showing the signal of D–C–D bonds at 2110 cm^{-1}. Middle, upon 24-h labeling in *C. elegans*, $PA\text{-}D_{31}$ signals are much lower than $OA\text{-}D_{34}$ signals in LDs, which are visualized by SRS at 2110 cm^{-1}. Scale bar: 20 µm. Right, the ratio between deuterium-labeled lipids and unlabeled total lipids (H-C-H 2850 cm^{-1}) in LDs is quantified and compared between PA and OA at both 12 h and 24 h, revealing a difference in incorporation rate between different fatty acids. Date are mean±s.d. (n=400–500 LDs). ***P<0.001 (one-way ANOVA). Graphs and images in panels D and E adapted with permission from Fu et al. (2014) (https://pubs.acs.org/doi/10.1021/ja504199s; further permission to reuse this figure should be directed to ACS). a.u., arbitrary units

an optimal CRS signal, the two beams need to be focused to the same focal point and have their pulses arrive at the same time. Careful alignment and the use of an optical delay line can ensure both requirements are met. The choice of pulse width is critical for effective coherent excitation. Once the spectral span of excitation pulse is close to the targeted Raman resonance, the efficiency will be optimal (Zumbusch et al., 2013). In biological samples, most Raman peaks obtain a spectral span of ∼10 cm^{-1}, therefore constraining the width of the pulses to be used. Such a pulse width can be achieved by using either picosecond lasers or femtosecond lasers that are shaped to meet the requirement of the spectral resolution (discussed below).

The choice of a laser-scanning microscope depends on whether its optimal transmission band covers the near infrared region. The detector of a CARS microscope captures the emission of anti-Stokes fluorescence. Given the blue-shifted wavelength of anti-Stokes photons, this configuration follows the example of a multiphoton fluorescence microscope, in which the emission fluorescence is separated from excitation light using a short-pass dichroic mirror and selected by a fluorescence filter before detection. In the case of CARS, a dichroic mirror and a filter are specifically chosen based on the wavelength of emitted anti-Stokes fluorescence (Zumbusch et al., 1999). By contrast, the detection of SRS signals follows a completely different and unique strategy since no photons of a new wavelength are generated. In the SRS process, the pump and the Stokes lasers experience an intensity loss and gain, respectively. To probe this pump or Stokes laser intensity change, a high frequency modulation transfer scheme is employed (Min et al., 2011). The intensity of one beam of excitation lasers (usually Stokes) is modulated at a high frequency *f*. Such a periodic presence of modulated beam results in a periodic switch-on of the SRS process. Therefore, the energy loss or gain in the other beam is modulated at the same frequency *f*. This small periodic intensity variation can then be demodulated and amplified by a lock-in amplifier that is referenced at the frequency *f*. Overall, CARS and SRS can utilize the same laser and microscope systems and be integrated to work simultaneously (Freudiger et al., 2008).

For a complex biological system, the existence of diverse chemical groups and their complex combination require CRS imaging at many different Raman peaks. To address this challenge, recent advances have been made, including multiplexing in CARS (Camp et al., 2014; Ideguchi et al., 2013; Pope et al., 2013) and SRS (Freudiger et al., 2011, 2014; Fu et al., 2012, 2013; Ozeki et al., 2012; Zhang et al., 2017a), which allow efficient image acquisition covering a wide range of Raman peaks. To build a CRS microscope with spectrum-scanning capability, the key technical requisite is a rapid switch of the resonant beating frequency of the pump and Stokes lasers. Conventionally, a change of the targeted Raman peak is achieved by tuning the wavelength of either the pump or Stokes beam. Such tuning mechanism involves a temperature change of nonlinear crystals, which limits the tuning speed and therefore its application in following fast *in vivo* dynamics of biological systems (Kong et al., 2013). In newly developed approaches, femtosecond lasers with broad spectral bandwidth are exploited to enable rapid wavelength changing. Different methods have been developed to achieve this goal (Zhang and Cheng, 2018; Zumbusch et al., 2013). The first method, and also the most straightforward one, is combining femtosecond and picosecond pulses directly and generating different beating frequencies in the femtosecond pulse (Camp et al., 2014; Zhang et al., 2017a). Once there are chemical bonds in resonance, both CARS and SRS processes will be activated at the corresponding frequency components in the femtosecond pulse. The spectral SRS signal can be detected by an array of photodiodes after different frequency components are separated by dispersion. Meanwhile, the generated broadband CARS signal can be detected by a spectrometer. The second method performs selective filtering on the femtosecond laser such that only the desired Raman peaks are excited (Freudiger et al., 2011; Fu et al., 2012). The third method utilizes two femtosecond lasers that are chirped, and the excitation of a specific Raman peak is determined by the temporal overlap between the two pulse trains, which can be achieved with an optical delay line. The spectrum of a sample is obtained by sequential image acquisition at different delays (Fu et al., 2013; Pope et al., 2013). The final approach is to sweep the laser source wavelength for fast switching of Raman resonance (Ozeki et al., 2012). A comparison between these different technology approaches is provided in Table 1.

CRS imaging of different lipid parameters *in vivo*

The crucial impact of lipids on metabolic health is associated with their quantity, composition, distribution and dynamics. Emerging advances of CRS microscopy bring tremendous opportunity for the imaging, quantification and tracking of lipids. Various methods exploiting the advantages of CRS microscopy have been developed to facilitate different purposes in lipid research. Here, we will present four major applications, including *in vivo* quantification of the levels of total lipid content, visualization of lipid distribution and differentiation of lipid classes, as well as tracking of LD mobility. We will also discuss the potential of multimodal imaging systems that harness the power of both CRS and fluorescence microscopy.

Lipid quantity is a major parameter that correlates with different metabolic status, and can be influenced by both genetic and environmental factors. A systemic increase in lipid quantity can lead to obesity, while a systemic decrease results in lipodystrophy, which both are major risk factors of diverse metabolic and chronic morbidity, such as type II diabetes, cardiovascular diseases and cancer (Butler et al., 2020; Nordestgaard and Varbo, 2014; Taskinen, 2005). The ability to quantify lipid content levels *in vivo* at high resolution is critical for lipid research. Neutral lipids, including triacylglycerols and cholesterol esters stored in LDs, contain chains of fatty acids, which carry the symmetric stretching of aliphatic hydrocarbons with a Raman shift at 2845 cm^{-1} (Freudiger et al., 2008) (Fig. 2A). As noted above, the signal obtained by CRS microscopy shows an intensity dependence on the concentration of targeted molecules over a large range, and can be used for quantitative imaging (Freudiger et al., 2008; Masia et al., 2013) (Fig. 2B). Thus,

Table 1. Comparison between different coherent Raman scattering microscopy approaches

Laser	Detection	Spatial resolution	Temporal resolution	Reference
CARS				
Two ps lasers	PMT	Up to video rate	–	Evans et al., 2005
Multiplexed CARS				
Optical combs	Photodiode/APD	∼10 ms per pixel	–	Ideguchi et al., 2013
Ps-fs combination	Spectrometer	3.5 ms per pixel	–	Camp et al., 2014
SRS				
Two ps lasers	Photodiode	Up to video rate	–	Saar et al., 2010
Multiplexed SRS				
Chirped fs lasers	Photodiode	All at diffraction limit (∼300 nm)	2 µs per pixel×spectral points	Fu et al., 2013
Sweeping fs laser source	Photodiode	∼0.13 µs per pixel	–	Ozeki et al., 2012
Filtered fs lasers	Photodiode	2 µs per pixel	–	Fu et al., 2012

ps, picosecond; fs, femtosecond. Video rate is 30 frames per second.

by targeting the characteristic stretching energy from the fatty acid chain, CRS can directly quantify the level of total lipids without the need for any labeling in living cells, tissues and organisms (Bradley et al., 2016; Di Napoli et al., 2016; Freudiger et al., 2008; Wang et al., 2011) (Fig. 1D). In particular, the result of SRS-based quantification has been shown to be comparable to biochemical methods, such as triacylglycerol colorimetric measurement or chromatography coupled with mass spectrometry analyses (Lin and Wang, 2017; Mutlu et al., 2020; Wang et al., 2011) (Fig. 2C). The spatial resolution of CRS microscopy is optical diffraction limited in three dimensions, which makes it feasible to quantitatively measure the morphological parameters of a single LD and their changes in response to different environmental inputs (Cao et al., 2016; Di Napoli et al., 2016). Additionally, owing to utilization of near-infrared band excitation lasers (typically 805 nm for pump and 1045 nm for Stokes), CRS is suitable for long term *in vivo* imaging owing to its non-photo bleaching and low phototoxicity (Cao et al., 2016; Di Napoli et al., 2016; Freudiger et al., 2008), and offers deep-tissue imaging capacity up to 200–400 µm (Hill et al., 2020). The imaging depth can be further improved by using tissue clearing methods (Li et al., 2019b; Wei et al., 2019). Furthermore, for a transparent organism, such as *Caenorhabditis elegans*, CRS can easily reveal lipid content levels of different tissues at a single-LD resolution in live animals quantitatively, whereas for non-transparent organisms, such as *Drosophila melanogaster* and *Mus musculus*, lipid distribution can be visualized and quantified in dissected tissues in a label-free and fixation-free manner (Fig. 1D) (Dou et al., 2012; Ji et al., 2013; Wang et al., 2011; Yu et al., 2014).

Lipid classes are diverse, with different chemical structures and biological functions (Tvrzicka et al., 2011). The ability to image different lipid classes, revealing their distribution and quantifying their composition is critically important for the understanding of LD-associated biology. CRS microscopy offers such an ability *in vivo*, as it is able to differentiate lipid classes based on their characteristic Raman signals at the single LD level. Fatty acids, the fundamental building blocks of lipids, can be categorized into saturated and unsaturated fatty acids, depending on the presence of C=C double bonds in their hydrocarbon tails. Distinct from the Raman peak of the CH_2 group at 2845 cm^{-1}, the =C–H bond associated with C=C bonds in unsaturated fatty acids presents a Raman peak at 3015 cm^{-1} (Bradley et al., 2016; Freudiger et al., 2008). Therefore, the ratio between 3015 and 2845 cm^{-1} can serve as an index of the degree of unsaturation in lipids. In addition, triacylglycerol and cholesterol ester are two major neutral lipids stored in LDs. Despite their distinctive physiological and pathological functions, it has been difficult to tell them apart *in vivo*, but two SRS-based approaches have been developed to differentiate cholesterol ester from triacylglycerol. The first approach turned to the fingerprint region, the low energy regime of the Raman spectrum, and targeted the C=C bond to distinguish these two classes of neutral lipids (Wang et al., 2013). This bond exhibits two distinct Raman peaks, 1655 cm^{-1} and 1669 cm^{-1}, in triacylglycerol and cholesterol ester, respectively, because of its location difference. The second approach applied hyperspectral SRS and utilized the ratio between Raman shifts of 3015 and 2965 cm^{-1} to differentiate between triacylglycerol and cholesterol ester (Fu et al., 2014) (Fig. 2D). At these two Raman shifts of the spectra, triacylglycerol and cholesterol ester exhibit the largest intensity difference in the opposite direction. Therefore, the ratio offers an effective way to quantitatively calculate the percentage of triacylglycerol and cholesterol ester in a sample and reveal the tissue-specific preference of these two neutral lipids in LDs (Fu et al., 2014).

Furthermore, deuterium isotope labeling can be integrated with CRS microscopy to enhance its specificity in order to track the temporal dynamics and spatial distribution of different lipids. The frequency of vibration is not only determined by the strength of the chemical bond, but also the masses of the atoms that form the bond. Isotope labeling therefore can shift the Raman signal of a chemical group and generate characteristic Raman peaks. Deuterium labeling is particularly useful because deuterated molecules can be utilized by the cells, making them almost identical to the target molecule in function. Specifically, the C-D bond in deuterated lipids presents a Raman peak at approximately 2110 cm^{-1}, in a region without any endogenous Raman signals from biological samples (Bradley et al., 2019; Fu et al., 2014). Using deuterium labeling, saturated palmitic acid, monounsaturated oleic acid and polyunsaturated arachidonic acid can be specifically tracked in time and space during their incorporation into LDs (Fu et al., 2014; Li et al., 2019a; Shen et al., 2017) (Fig. 2E). Compared to unsaturated fatty acids, saturated fatty acids exhibit a delayed incorporation into LDs and accumulate in the ER, resulting in the membrane abnormality (Fu et al., 2014; Shen et al., 2017). In addition, through following the accumulation of deuterated oleic acids into LDs by CRS, the rate of lipid biosynthesis can be quantified in live cells and organisms (Lin and Wang, 2017; Mutlu et al., 2020; Yu et al., 2017). Conversely, upon the removal of deuterium labeling, the decay of deuterated lipid signals from LDs can determine the rate of lipid mobilization (Lin and Wang, 2017; Mutlu et al., 2020; Yu et al., 2017). This method of deuterium addition and removal can track the dynamic balance between lipid biosynthesis and mobilization *in vivo* at the LD level, and thus reveal how this balance is fine-tuned by the interaction between genes and the environment (Fu et al., 2014; Lin and Wang, 2017; Mutlu et al., 2020). For example, when exposed to bacteria cultured in a methionine-deficient environment, the host *C. elegans* increases fat storage by twofold, which is mediated by the nuclear hormone receptor NHR-25 (LRH1 in mammals) (Lin and Wang, 2017). Interestingly, through deuterium-SRS tracing, it was shown that bacterial signals lead to both increased lipid synthesis and decreased lipid mobilization in the host worms, but NHR-25 only mediates the effect on lipid mobilization (Lin and Wang, 2017). Furthermore, deuterated cholesterol has been used for selective imaging of intracellular cholesterol storage, which reveals the preference of some LDs for the storage of cholesterol ester versus triacylglycerol (Alfonso-García et al., 2015).

LDs are not static but are mobile organelles, and their mobility aids the growth and breakdown of LDs, as well as their interactions with other organelles (Kilwein and Welte, 2019; Kumar et al., 2019; Welte, 2009). Several theoretical models have been built to describe the biological impact from the physical perspective of LD mobility. In addition to its ability of imaging live cells, the high sensitivity of CRS permits rapid imaging of lipids at up to 30 frames per second (with a resonant scanner), therefore offering an excellent opportunity to monitor LD locomotion and examine those theoretical models. For instance, exploiting the high speed and resolution of SRS microscopy made it possible to track the motion of single LDs (Dou et al., 2012; Kumar et al., 2019; Zhang et al., 2017b). Upon establishing pipelines for a quantitative analysis of LD mobility, the study revealed the correlation between the LD motion pattern and metabolic status statistically (Zhang et al., 2017b).

Furthermore, the surface of LDs contains a variety of proteins, which supports their formation, growth, breakdown and motility, mediates interactions with other organelles and contributes to LD heterogeneity (Olzmann and Carvalho, 2019; Thiam and Beller, 2017; Zhang and Liu, 2019). Through tagging with diverse

fluorescent proteins, these LD-associated proteins can be visualized by fluorescence microscopy with high sensitivity, specificity and resolution. CRS can be combined with fluorescence-imaging modality, such as in a confocal and multiphoton setup, to image lipids in the core of LDs alongside fluorescence-labeled proteins on the surface of LDs (Li et al., 2015; Na et al., 2015; Pope et al., 2013; Wang et al., 2011) (Fig. 1D). Moreover, LDs and other organelles that are marked by fluorescent tags can also be simultaneously imaged using such multi-modal imaging platforms (Li et al., 2015).

SRS-based screens to reveal lipid regulatory mechanisms

SRS microscopy provides a novel imaging method to analyze the quantity, distribution, composition and dynamics of LDs, with chemical specificity, subcellular resolution and video-rate speed. The ability to image live cells and organisms also opens the door for functional genetics to discover new genes and mechanisms that regulate different parameters of lipid metabolism. These regulatory genes can be considered the 'throttle' and 'brakes' in lipid metabolism; they respond to the instantaneous status of metabolism and/or the environment and cooperate to control lipid dynamics, and their alteration can result in differences in phenotypes. Integration of SRS microscopy and functional genetics offers a powerful way to systemically discover genes and their pathways that are involved in regulating specific lipid phenotypes in a high-throughput manner. There are two major screening strategies in functional genetics, forward genetic screens and reverse genetic screens. A forward genetic screen starts with the identification of mutants with particular phenotypes, which is followed by determining the genes responsible for the mutants (Kutscher and Shaham, 2014). By contrast, a reverse genetic screen starts with a known list of genes and analyzes the phenotypes that are associated with their modifications (Boulin and Hobert, 2012). *C. elegans* is a model organism that is commonly used in both types of screens, as it has rapid life cycle and ease of genetic manipulation (Jorgensen and Mango, 2002). The whole-body transparency and small size of *C. elegans* also make them well suited for screening by using optical microscopy. In addition, *C. elegans* shares all the major lipid metabolism pathways with humans (Kaletta and Hengartner, 2006). In recent years, SRS microscopy has proven powerful for both types of screening strategies in *C. elegans* and has been used to discover new regulatory genes and mechanisms involved in lipid dynamics.

SRS microscopy was first examined for its screening ability in reverse genetics using RNA interference (RNAi), in which 272 genes encoding cell surface receptors and nuclear hormone receptors were knocked down by RNAi in *C. elegans* (Wang et al., 2011). Through the screen, nine genes whose RNAi inactivation increased the total lipid content levels were identified (Wang et al., 2011). In another reverse genetic screen of chemosensory neuronal mutants using SRS, specific olfactory neurons were discovered to regulate lipid mobilization in *C. elegans*, and further screens aided the delineation of the neuroendocrine signaling pathway that links olfactory perception and peripheral lipid metabolism (Mutlu et al., 2020).

However, forward genetic screens using a laser-scanning microscope setup such as in SRS have traditionally been less accessible and more difficult than reverse genetic screens. In a forward genetic screen, the few positive candidates need to be recognized and recovered from thousands of mutant worms. Therefore, when using a laser-scanning microscope, mutant worms have to be imaged either individually or in a small group on a slide, which is a time-consuming and labor-intensive processes. To increase the screening throughout and speed, a photo-highlighting strategy was developed in which a transgenic strain expressing a photoswitchable protein that changes the color from green to red upon the 405 nm blue light illumination was generated, making it possible to image hundreds of worms together and photo-highlight positive candidates into red for easy recovery (Yu et al., 2017). Using this strategy, ∼50,000 mutants derived from ethyl methanesulfonate mutagenesis were imaged by SRS microscopy, and 57 mutants that exhibited different phenotypes with regard to the content, number, size and distribution of LDs were isolated (Yu et al., 2017). Further analysis of four mutants that showed a decreased number and content of LDs revealed that the genes responsible encode key components in the bone morphogenetic protein (BMP) pathway. Through deuterium-SRS tracing, it was shown that these BMP mutants have increased lipid mobilization, which is consistent with their effects on increasing mitochondrial β-oxidation gene expression and promoting mitochondrial fusion (Yu et al., 2017).

Besides genetic screens, SRS microscopy can also be applied to search for nutritional and chemical factors in the environment that influence lipid dynamics. For example, in the same study that reports the olfactory regulation of lipid metabolism, SRS microscopy was also used to pinpoint a specific odor-triggering lipid accumulation from a group of volatile molecules (Mutlu et al., 2020). Another study employed an SRS-based screen of all amino acids, leading to the discovery of methionine as an environmental input that influences bacterial methyl cycle and consequently host lipid metabolism (Lin and Wang, 2017). Together, these SRS-based screens have provided new insights into the biological mechanisms underlying the regulation of lipid dynamics.

SRS application in understanding disease-related lipid pathology

SRS microscopy also represents a new chemical imaging method that can be used to understand the link between reprogramming of lipid metabolism and disease pathology. Lipid metabolism is essential to support fundamental biological activities and its abnormalities both directly and indirectly contribute to many pathological processes, such as obesity, neurodegeneration, fatty-liver diseases and cancer (Butler et al., 2020; Fu et al., 2014; Liu et al., 2015; Marschallinger et al., 2020). Hyperspectral SRS has been used to examine the leptin-deficient *ob/ob* mouse, which is obese due to excessive food intake, and found that the expansion of LDs in the *ob/ob* mouse is predominantly due to accumulation of triacylglycerol but not cholesterol ester (Fu et al., 2014). The same study also reported that a triacylglycerol-specific increase contributes to LD expansion in nonalcoholic fatty liver induced by tunicamycin injection (Fu et al., 2014). Interestingly, in both cases, increased deposition of unsaturated lipids was detected in the rapidly expanded LDs, which might lead to an imbalance of saturated versus unsaturated lipids in other compartments of the cell and so cause lipotoxicity (Fu et al., 2014). Furthermore, lipid metabolism also plays a crucial role in the onset and progression of cancer. It is known that obesity is a major risk factor for cancer, and elevated lipid biosynthesis highly correlates with carcinogenesis and tumor development (Menendez and Lupu, 2007). Excitingly, studies using SRS-based imaging approaches have revealed an alteration in lipid composition as another vital attribution to cancer pathology. In prostate cancer, abnormal accumulation of cholesterol ester in LDs is associated with high-grade cancer and metastases, as shown by using SRS microscopy together with Raman spectroscopy (Li et al., 2016; Yue et al., 2014). Further analyses revealed that abolishing cholesterol ester accumulation reduces cancer proliferation, invasion, tumor growth and metastasis (Li et al., 2016; Yue et al., 2014). In ovarian cancer,

Journal of Cell Science (2022) 135, jcs252353. doi:10.1242/jcs.252353

Box. 1. Innovations in CRS cytometry

The implementation of cytometry function in CRS requires highly efficient spectral information acquisition and a flow interface that can be accommodated on CRS microscope. Two main approaches have been taken to achieve rapid spectral acquisition.

- The first approach is to combine femtosecond and picosecond pulses for simultaneous spectral acquisition (Zhang et al., 2017a) with a photodiode array.
- The second approach utilizes a fast-tuning filter based on the angle of grating in the Stokes beam. By well-controlled filtering sequence synchronized with imaging acquisition, the four Raman peaks are selectively activated and switched within about 100 ns (Nitta et al., 2020; Suzuki et al., 2019).

The utilization of line scan technique (Nitta et al., 2020; Suzuki et al., 2019; Zhang et al., 2017a) provides fast image acquisition when cells flow through microfluidic channels. At the same time, home-built microfluidic channels are developed to provide a suitable interface between CRS microscope and flowing cells suspension (Nitta et al., 2020; Suzuki et al., 2019). Moreover, acoustic standing waves confine cells in the center of the microfluidic channel, and thus in focus throughout the entire sorting process, ensuring consistent high-quality images (Nitta et al., 2020; Suzuki et al., 2019). With these technical advancements, the CRS flow cytometry can sort different cell types at a flow rate of ∼140 cells/s, and selectively collected HT29 cells (mimicking circulating tumor cells) out of an artificial multi-cell mixture (Suzuki et al., 2019).

Box. 2. Current limitations of CRS microscopy

- The detection sensitivity is typically ∼1 mM. It is thus challenging to image lipid molecules of low abundance.
- The spatial resolution is currently ∼300 nm, but nascent LDs have a size below this limit.
- The laser system requires modifications of alignment, pulse shaping or modulation (or all of these) to serve as an excitation source.
- The detection unit of an SRS microscope includes a photodiode, lock-in amplifier and function generator. However, for the installation and wiring of these electronic components, there is no off the shelf solution to date. Furthermore, for some types of hyperspectral SRS, photodiode and lock-in amplifier arrays are required.
- Despite commercially available components, researchers need to assemble them into a single operating system. However, without a unified user interface available, the communication and synchronization of different components require frequent maintenance for daily use.
- Currently, hyperspectral CRS is able to only detect three to four chemical groups; this is limiting and insufficient considering the complexity of molecules, for example, lipid variants. Several factors contribute to this limitation: (1) the low detection sensitivity makes it difficult to extract chemical groups present in low concentration; (2) the relatively long acquisition time challenges the extraction of chemical groups that are highly dynamic or have a large flux; (3) the limited signal-to-noise ratio (SNR) hinders the deconvolution of hyperspectral data.

an increased level of unsaturated lipids in LDs can be detected in cancer stem cells by using hyperspectral SRS imaging of single cells (Li et al., 2017). Importantly, genetic or pharmaceutical inhibition of fatty acid desaturases is sufficient to prevent the formation of spheres of ovarian cancer stem cells in cell culture, which indicates reduced mobility and increased attachment (Li et al., 2017). Consistent with this, these treated stem cells exhibit a decreased capacity to initiate tumors in mice. These studies demonstrate the power of SRS imaging in discovering new biomarkers of diseases and driving mechanistic understanding of their pathology, as well leading towards the development of better treatments. Owing to recent technical innovations with regard to SRS imaging flow cytometry (see Box 1), thousands of cells can now be sorted in a short time by probing different chemical vibrations (Nitta et al., 2020; Suzuki et al., 2019), which further strengthens the power of this imaging modality by providing a high-throughput, high-content capacity.

Perspectives

CRS probes lipid molecules owing to the presence of several characteristic chemical groups. It provides label-free quantification of LDs *in vivo*, and the high spatial and temporal resolution allows the investigation of the dynamics of LD metabolism. An increasing adoption of CRS in LD research is expanding our knowledge of LD biology and its implications. In combination with genetics, CRS has shown great potential in searching for novel regulators of LD metabolism, as well as elucidating the underlying molecular mechanisms. Biomedical application of CRS imaging also paves the way to understanding the mechanistic link between LD abnormality and disease onset and progression, leading to new approaches for prevention and treatment. Despite the advantages of CRS, it will be necessary to remove some of the current hurdles before its wider application in the field of LD research (see Box 2). For instance, the detection sensitivity of CRS is typically ∼1 mM and the spatial resolution ∼300 nm, which both need to be further improved to probe lipid molecules of low abundance and nascent LDs with a size below this diffraction limit. In addition, the deconvolution of hyperspectral SRS data needs to be improved to provide more molecular features, such as sphingolipids, oligosaccharides and protein lipidation. Importantly, CRS microscopes are still a few steps away from being a turn-key system. The difficulties include customization of the laser system, manual alignment optics, home-building detection units and non-unified user interfaces, thus hindering the deployment of this imaging modality in general biology and biomedical labs. Future technical innovations are expected to tackle these challenges, through advancement in new laser sources, and detection hardware and data analysis algorithms, as well as ingenious integration of different components for easy and budget-friendly implementation. Recent studies have made promising progress in these areas, such as the use of deep learning for signal recovery and analyses (Manifold et al., 2019; Zhang et al., 2020) and tissue clearing for deeper imaging (Li et al., 2019b; Wei et al., 2019), both of which have proven to offer enhanced performance. Fully integrated CRS microscopy systems are also becoming commercially available. Further breakthroughs are on the horizon, and we anticipate they will unleash the full power of this chemical-imaging method, leading to new applications and discoveries in LD research and beyond.

Acknowledgements

We thank Dr Dinghuan Deng, Dr Sena Mutlu and Dr Qian Zhao for fruitful discussion. We apologize to the authors whose work could not be cited because of space constraints.

Competing interests

The authors declare no competing or financial interests.

Funding

We thank the National Institutes of Health (NIH) [grants R01AG045183 (M.C.W.), R01AT009050 (M.C.W.), R01AG062257 (M.C.W.) and DP1DK113644 (M.C.W.)], Howard Hughes Medical Institute (M.C.W.) and the Welch Foundation (M.C.W.) for funding our work in this area. Deposited in PMC for release after 12 months.

References

Alfonso-García, A., Pfisterer, S. G., Riezman, H., Ikonen, E. and Potma, E. O. (2015). D38-cholesterol as a Raman active probe for imaging intracellular cholesterol storage. *J. Biomed. Opt.* **21**, 061003. doi:10.1117/1.JBO.21.6.061003

Boulin, T. and Hobert, O. (2012). From genes to function: the C. elegans genetic toolbox. *Wiley Interdiscip. Rev. Dev. Biol.* **1**, 114-137. doi:10.1002/wdev.1
Bradley, J., Pope, I., Masia, F., Sanusi, R., Langbein, W., Swann, K. and Borri, P. (2016). Quantitative imaging of lipids in live mouse oocytes and early embryos using CARS microscopy. *Development* **143**, 2238-2247. doi:10.1242/dev.129908
Bradley, J., Pope, I., Wang, Y., Langbein, W., Borri, P. and Swann, K. (2019). Dynamic label-free imaging of lipid droplets and their link to fatty acid and pyruvate oxidation in mouse eggs. *J. Cell Sci.* **132**, jcs228999. doi:10.1242/jcs.228999
Brasaemle, D. L., Barber, T., Wolins, N. E., Serrero, G., Blanchette-Mackie, E. J. and Londos, C. (1997). Adipose differentiation-related protein is an ubiquitously expressed lipid storage droplet-associated protein. *J. Lipid Res.* **38**, 2249-2263. doi:10.1016/S0022-2275(20)34939-7
Bustos, V. and Partridge, L. (2017). Good Ol' fat: links between lipid signaling and longevity. *Trends Biochem. Sci.* **42**, 812-823. doi:10.1016/j.tibs.2017.07.001
Butler, L. M., Perone, Y., Dehairs, J., Lupien, L. E., de Laat, V., Talebi, A., Loda, M., Kinlaw, W. B. and Swinnen, J. V. (2020). Lipids and cancer: emerging roles in pathogenesis, diagnosis and therapeutic intervention. *Adv. Drug Deliv. Rev.* **159**, 245-293. doi:10.1016/j.addr.2020.07.013
Camp, C. H., Jr. and Cicerone, M. T. (2015). Chemically sensitive bioimaging with coherent Raman scattering. *Nat. Photonics* **9**, 295-305. doi:10.1038/nphoton.2015.60
Camp, C. H., Jr., Lee, Y. J., Heddleston, J. M., Hartshorn, C. M., Walker, A. R. H., Rich, J. N., Lathia, J. D. and Cicerone, M. T. (2014). High-speed coherent Raman fingerprint imaging of biological tissues. *Nat. Photonics* **8**, 627-634. doi:10.1038/nphoton.2014.145
Cao, C., Zhou, D., Chen, T., Streets, A. M. and Huang, Y. (2016). Label-free digital quantification of lipid droplets in single cells by stimulated raman microscopy on a microfluidic platform. *Anal. Chem.* **88**, 4931-4939. doi:10.1021/acs.analchem.6b00862
Cheng, J.-X. and Xie, X. S. (2015). Vibrational spectroscopic imaging of living systems: an emerging platform for biology and medicine. *Science* **350**, aaa8870. doi:10.1126/science.aaa8870
Cui, L. and Liu, P. (2020). Two types of contact between lipid droplets and mitochondria. *Front. Cell Dev. Biol.* **8**, 618322. doi:10.3389/fcell.2020.618322
Débarre, D., Supatto, W., Pena, A.-M., Fabre, A., Tordjmann, T., Combettes, L., Schanne-Klein, M.-C. and Beaurepaire, E. (2006). Imaging lipid bodies in cells and tissues using third-harmonic generation microscopy. *Nat. Methods* **3**, 47-53. doi:10.1038/nmeth813
Di Napoli, C., Pope, I., Masia, F., Langbein, W., Watson, P. and Borri, P. (2016). Quantitative spatiotemporal chemical profiling of individual lipid droplets by hyperspectral CARS microscopy in living human adipose-derived stem cells. *Anal. Chem.* **88**, 3677-3685. doi:10.1021/acs.analchem.5b04468
Ding, Y., Zhang, S., Yang, L., Na, H., Zhang, P., Zhang, H., Wang, Y., Chen, Y., Yu, J., Huo, C. et al. (2013). Isolating lipid droplets from multiple species. *Nat. Protoc.* **8**, 43-51. doi:10.1038/nprot.2012.142
Djambazova, K. V., Klein, D. R., Migas, L. G., Neumann, E. K., Rivera, E. S., Van de Plas, R., Caprioli, R. M. and Spraggins, J. M. (2020). Resolving the complexity of spatial lipidomics using MALDI TIMS imaging mass spectrometry. *Anal. Chem.* **92**, 13290-13297. doi:10.1021/acs.analchem.0c02520
Dou, W., Zhang, D., Jung, Y., Cheng, J.-X. and Umulis, D. M. (2012). Label-free imaging of lipid-droplet intracellular motion in early *Drosophila* embryos using femtosecond-stimulated Raman loss microscopy. *Biophys. J.* **102**, 1666-1675. doi:10.1016/j.bpj.2012.01.057
Evans, C. L. and Xie, X. S. (2008). Coherent anti-stokes raman scattering microscopy: chemical imaging for biology and medicine. *Annu. Rev. Anal. Chem.* **1**, 883-909. doi:10.1146/annurev.anchem.1.031207.112754
Evans, C. L., Potma, E. O., Puoris'haag, M., Cote, D., Lin, C. P. and Xie, X. S. (2005). Chemical imaging of tissue in vivo with video-rate coherent anti-Stokes Raman scattering microscopy. *Proc. Natl. Acad. Sci. USA* **102**, 16807-16812. doi:10.1073/pnas.0508282102
Fam, T., Klymchenko, A. and Collot, M. (2018). Recent advances in fluorescent probes for lipid droplets. *Materials* **11**, 1768. doi:10.3390/ma11091768
Freudiger, C. W., Min, W., Saar, B. G., Lu, S., Holtom, G. R., He, C., Tsai, J. C., Kang, J. X. and Xie, X. S. (2008). Label-free biomedical imaging with high sensitivity by stimulated Raman scattering microscopy. *Science* **322**, 1857-1861. doi:10.1126/science.1165758
Freudiger, C. W., Min, W., Holtom, G. R., Xu, B., Dantus, M. and Sunney Xie, X. (2011). Highly specific label-free molecular imaging with spectrally tailored excitation-stimulated Raman scattering (STE-SRS) microscopy. *Nat. Photonics* **5**, 103-109. doi:10.1038/nphoton.2010.294
Freudiger, C. W., Yang, W., Holtom, G. R., Peyghambarian, N., Xie, X. S. and Kieu, K. Q. (2014). Stimulated Raman scattering microscopy with a robust fibre laser source. *Nat. Photonics* **8**, 153-159. doi:10.1038/nphoton.2013.360
Fu, D., Lu, F.-K., Zhang, X., Freudiger, C., Pernik, D. R., Holtom, G. and Xie, X. S. (2012). Quantitative chemical imaging with multiplex stimulated Raman scattering microscopy. *J. Am. Chem. Soc.* **134**, 3623-3626. doi:10.1021/ja210081h
Fu, D., Holtom, G., Freudiger, C., Zhang, X. and Xie, X. S. (2013). Hyperspectral imaging with stimulated raman scattering by chirped femtosecond lasers. *J. Phys. Chem. B* **117**, 4634-4640. doi:10.1021/jp308938t
Fu, D., Yu, Y., Folick, A., Currie, E., Farese, R. V., Tsai, T.-H., Xie, X. S. and Wang, M. C. (2014). In vivo metabolic fingerprinting of neutral lipids with hyperspectral stimulated raman scattering microscopy. *J. Am. Chem. Soc.* **136**, 8820-8828. doi:10.1021/ja504199s
Ganikhanov, F., Evans, C. L., Saar, B. G. and Xie, X. S. (2006). High-sensitivity vibrational imaging with frequency modulation coherent anti-Stokes Raman scattering (FM CARS) microscopy. *Opt. Lett.* **31**, 1872. doi:10.1364/OL.31.001872
Gao, Q. and Goodman, J. M. (2015). The lipid droplet—a well-connected organelle. *Front. Cell Dev. Biol.* **3**, 49. doi:10.3389/fcell.2015.00049
Herker, E., Vieyres, G., Beller, M., Krahmer, N. and Bohnert, M. (2021). Lipid droplet contact sites in health and disease. *Trends Cell Biol.* **31**, 345-358. doi:10.1016/j.tcb.2021.01.004
Hill, A. H., Munger, E., Francis, A. T., Manifold, B. and Fu, D. (2019). Frequency modulation stimulated raman scattering microscopy through polarization encoding. *J. Phys. Chem. B* **123**, 8397-8404. doi:10.1021/acs.jpcb.9b07075
Hill, A. H., Manifold, B. and Fu, D. (2020). Tissue imaging depth limit of stimulated Raman scattering microscopy. *Biomed. Opt. Express* **11**, 762. doi:10.1364/BOE.382396
Ideguchi, T., Holzner, S., Bernhardt, B., Guelachvili, G., Picqué, N. and Hänsch, T. W. (2013). Coherent Raman spectro-imaging with laser frequency combs. *Nature* **502**, 355-358. doi:10.1038/nature12607
Jarc, E. and Petan, T. (2020). A twist of FATe: lipid droplets and inflammatory lipid mediators. *Biochimie* **169**, 69-87. doi:10.1016/j.biochi.2019.11.016
Ji, M., Orringer, D. A., Freudiger, C. W., Ramkissoon, S., Liu, X., Lau, D., Golby, A. J., Norton, I., Hayashi, M., Agar, N. Y. R. et al. (2013). Rapid, label-free detection of brain tumors with stimulated Raman scattering microscopy. *Sci. Transl. Med.* **5**, 201ra119. doi:10.1126/scitranslmed.3005954
Jones, R. R., Hooper, D. C., Zhang, L., Wolverson, D. and Valev, V. K. (2019). Raman techniques: fundamentals and frontiers. *Nanoscale Res. Lett.* **14**, 231. doi:10.1186/s11671-019-3039-2
Jorgensen, E. M. and Mango, S. E. (2002). The art and design of genetic screens: Caenorhabditis elegans. *Nat. Rev. Genet.* **3**, 356-369. doi:10.1038/nrg794
Kaletta, T. and Hengartner, M. O. (2006). Finding function in novel targets: *C. elegans* as a model organism. *Nat. Rev. Drug Discov.* **5**, 387-399. doi:10.1038/nrd2031
Kilwein, M. D. and Welte, M. A. (2019). Lipid droplet motility and organelle contacts. *Contact* **2**, 251525641989568. doi:10.1177/2515256419895688
Kim, K., Lee, S., Yoon, J., Heo, J., Choi, C. and Park, Y. (2016). Three-dimensional label-free imaging and quantification of lipid droplets in live hepatocytes. *Sci. Rep.* **6**, 36815. doi:10.1038/srep36815
Kong, L., Ji, M., Holtom, G. R., Fu, D., Freudiger, C. W. and Xie, X. S. (2013). Multicolor stimulated Raman scattering microscopy with a rapidly tunable optical parametric oscillator. *Opt. Lett.* **38**, 145. doi:10.1364/OL.38.000145
Kuerschner, L., Ejsing, C. S., Ekroos, K., Shevchenko, A., Anderson, K. I. and Thiele, C. (2005). Polyene-lipids: a new tool to image lipids. *Nat. Methods* **2**, 39-45. doi:10.1038/nmeth728
Kuerschner, L., Moessinger, C. and Thiele, C. (2008). Imaging of lipid biosynthesis: how a neutral lipid enters lipid droplets. *Traffic* **9**, 338-352. doi:10.1111/j.1600-0854.2007.00689.x
Kumar, M., Ojha, S., Rai, P., Joshi, A., Kamat, S. S. and Mallik, R. (2019). Insulin activates intracellular transport of lipid droplets to release triglycerides from the liver. *J. Cell Biol.* **218**, 3697-3713. doi:10.1083/jcb.201903102
Kutscher, L. M. and Shaham, S. (2014). Forward and reverse mutagenesis in C. elegans. In *WormBook*, ed. *The C. elegans* Research Community, WormBook, http://www.wormbook.org. doi:10.1895/wormbook.1.167.1
Lass, A., Zimmermann, R., Oberer, M. and Zechner, R. (2011). Lipolysis - A highly regulated multi-enzyme complex mediates the catabolism of cellular fat stores. *Prog. Lipid Res.* **50**, 14-27. doi:10.1016/j.plipres.2010.10.004
Li, X., Lam, W. J., Cao, Z., Hao, Y., Sun, Q., He, S., Mak, H. Y. and Qu, J. Y. (2015). Integrated femtosecond stimulated Raman scattering and two-photon fluorescence imaging of subcellular lipid and vesicular structures. *J. Biomed. Opt.* **20**, 110501. doi:10.1117/1.JBO.20.11.110501
Li, J., Gu, D., Lee, S. S.-Y., Song, B., Bandyopadhyay, S., Chen, S., Konieczny, S. F., Ratliff, T. L., Liu, X., Xie, J. et al. (2016). Abrogating cholesterol esterification suppresses growth and metastasis of pancreatic cancer. *Oncogene* **35**, 6378-6388. doi:10.1038/onc.2016.168
Li, J., Condello, S., Thomes-Pepin, J., Ma, X., Xia, Y., Hurley, T. D., Matei, D. and Cheng, J.-X. (2017). Lipid desaturation is a metabolic marker and therapeutic target of ovarian cancer stem cells. *Cell Stem Cell* **20**, 303-314.e5. doi:10.1016/j.stem.2016.11.004
Li, X., Li, Y., Jiang, M., Wu, W., He, S., Chen, C., Qin, Z., Tang, B. Z., Mak, H. Y. and Qu, J. Y. (2019a). Quantitative imaging of lipid synthesis and lipolysis dynamics in caenorhabditis elegans by stimulated raman scattering microscopy. *Anal. Chem.* **91**, 2279-2287. doi:10.1021/acs.analchem.8b04875
Li, J., Lin, P., Tan, Y. and Cheng, J.-X. (2019b). Volumetric stimulated Raman scattering imaging of cleared tissues towards three-dimensional chemical histopathology. *Biomed. Opt. Express* **10**, 4329. doi:10.1364/BOE.10.004329

Lin, C.-C. J. and Wang, M. C. (2017). Microbial metabolites regulate host lipid metabolism through NR5A–Hedgehog signalling. *Nat. Cell Biol.* **19**, 550-557. doi:10.1038/ncb3515
Lincoln, C. N., Fitzpatrick, A. E. and van Thor, J. J. (2012). Photoisomerisation quantum yield and non-linear cross-sections with femtosecond excitation of the photoactive yellow protein. *Phys. Chem. Chem. Phys.* **14**, 15752. doi:10.1039/c2cp41718a
Listenberger, L. L. and Brown, D. A. (2007). Fluorescent detection of lipid droplets and associated proteins. *Curr. Protoc. Cell Biol.* **35**, 24.2.1-24.2.11. doi:10.1002/0471143030.cb2402s35
Liu, L., Zhang, K., Sandoval, H., Yamamoto, S., Jaiswal, M., Sanz, E., Li, Z., Hui, J., Graham, B. H., Quintana, A. et al. (2015). Glial lipid droplets and ROS induced by mitochondrial defects promote neurodegeneration. *Cell* **160**, 177-190. doi:10.1016/j.cell.2014.12.019
Manifold, B., Thomas, E., Francis, A. T., Hill, A. H. and Fu, D. (2019). Denoising of stimulated Raman scattering microscopy images via deep learning. *Biomed. Opt. Express* **10**, 3860. doi:10.1364/BOE.10.003860
Marschallinger, J., Iram, T., Zardeneta, M., Lee, S. E., Lehallier, B., Haney, M. S., Pluvinage, J. V., Mathur, V., Hahn, O., Morgens, D. W. et al. (2020). Lipid-droplet-accumulating microglia represent a dysfunctional and proinflammatory state in the aging brain. *Nat. Neurosci.* **23**, 194-208. doi:10.1038/s41593-019-0566-1
Masia, F., Glen, A., Stephens, P., Borri, P. and Langbein, W. (2013). Quantitative chemical imaging and unsupervised analysis using hyperspectral coherent anti-stokes Raman scattering microscopy. *Anal. Chem.* **85**, 10820-10828. doi:10.1021/ac402303g
Menendez, J. A. and Lupu, R. (2007). Fatty acid synthase and the lipogenic phenotype in cancer pathogenesis. *Nat. Rev. Cancer* **7**, 763-777. doi:10.1038/nrc2222
Min, W., Freudiger, C. W., Lu, S. and Xie, X. S. (2011). Coherent nonlinear optical imaging: beyond fluorescence microscopy. *Annu. Rev. Phys. Chem.* **62**, 507-530. doi:10.1146/annurev.physchem.012809.103512
Mutlu, A. S., Gao, S. M., Zhang, H. and Wang, M. C. (2020). Olfactory specificity regulates lipid metabolism through neuroendocrine signaling in Caenorhabditis elegans. *Nat. Commun.* **11**, 1450. doi:10.1038/s41467-020-15296-8
Na, H., Zhang, P., Chen, Y., Zhu, X., Liu, Y., Liu, Y., Xie, K., Xu, N., Yang, F., Yu, Y. et al. (2015). Identification of lipid droplet structure-like/resident proteins in Caenorhabditis elegans. *Biochim. Biophys. Acta (BBA) Mol. Cell Res.* **1853**, 2481-2491. doi:10.1016/j.bbamcr.2015.05.020
Nagli, L., Gaft, M., Fleger, Y. and Rosenbluh, M. (2008). Absolute Raman cross-sections of some explosives: trend to UV. *Opt. Mater.* **30**, 1747-1754. doi:10.1016/j.optmat.2007.11.019
Nitta, N., Iino, T., Isozaki, A., Yamagishi, M., Kitahama, Y., Sakuma, S., Suzuki, Y., Tezuka, H., Oikawa, M., Arai, F. et al. (2020). Raman image-activated cell sorting. *Nat. Commun.* **11**, 3452. doi:10.1038/s41467-020-17285-3
Nordestgaard, B. G. and Varbo, A. (2014). Triglycerides and cardiovascular disease. *Lancet* **384**, 626-635. doi:10.1016/S0140-6736(14)61177-6
Ohsaki, Y., Suzuki, M. and Fujimoto, T. (2014). Open questions in lipid droplet biology. *Chem. Biol.* **21**, 86-96. doi:10.1016/j.chembiol.2013.08.009
Olzmann, J. A. and Carvalho, P. (2019). Dynamics and functions of lipid droplets. *Nat. Rev. Mol. Cell Biol.* **20**, 137-155. doi:10.1038/s41580-018-0085-z
Ozeki, Y., Umemura, W., Otsuka, Y., Satoh, S., Hashimoto, H., Sumimura, K., Nishizawa, N., Fukui, K. and Itoh, K. (2012). High-speed molecular spectral imaging of tissue with stimulated Raman scattering. *Nat. Photonics* **6**, 845-851. doi:10.1038/nphoton.2012.263
Pope, I., Langbein, W., Watson, P. and Borri, P. (2013). Simultaneous hyperspectral differential-CARS, TPF and SHG microscopy with a single 5 fs Ti:Sa laser. *Opt. Express* **21**, 7096. doi:10.1364/OE.21.007096
Saar, B. G., Freudiger, C. W., Reichman, J., Stanley, C. M., Holtom, G. R. and Xie, X. S. (2010). Video-rate molecular imaging in vivo with stimulated Raman scattering. *Science* **330**, 1368-1370. doi:10.1126/science.1197236
Shen, Y., Zhao, Z., Zhang, L., Shi, L., Shahriar, S., Chan, R. B., Di Paolo, G., Min, W., Di Paolo, G. and Min, W. (2017). Metabolic activity induces membrane phase separation in endoplasmic reticulum. *Proc. Natl. Acad. Sci. USA* **114**, 13394-13399. doi:10.1073/pnas.1712555114
Suzuki, Y., Kobayashi, K., Wakisaka, Y., Deng, D., Tanaka, S., Huang, C.-J. J., Lei, C., Sun, C.-W. W., Liu, H., Fujiwaki, Y. et al. (2019). Label-free chemical imaging flow cytometry by high-speed multicolor stimulated Raman scattering. *Proc. Natl. Acad. Sci. USA* **116**, 15842-15848. doi:10.1073/pnas.1902322116
Taskinen, M.-R. (2005). Type 2 Diabetes as a Lipid Disorder. *Curr. Mol. Med.* **5**, 297-308. doi:10.2174/1566524053766086
Thiam, A. R. and Beller, M. (2017). The why, when and how of lipid droplet diversity. *J. Cell Sci.* **130**, 315-324. doi:10.1242/jcs.192021
Thiam, A. R. and Dugail, I. (2019). Lipid droplet–membrane contact sites – from protein binding to function. *J. Cell Sci.* **132**, jcs230169. doi:10.1242/jcs.230169
Thiam, A. R. and Ikonen, E. (2021). Lipid droplet nucleation. *Trends Cell Biol.* **31**, 108-118. doi:10.1016/j.tcb.2020.11.006
Tian, Y.-J., Zuo, J., Zhang, L.-Y., Li, Z.-W., Gao, S.-Q. and Lu, G.-H. (2007). Study of resonance Raman cross section of aqueous β -carotene at low concentrations. *Appl. Phys. B* **87**, 727-730. doi:10.1007/s00340-007-2633-7
Tvrzicka, E., Kremmyda, L.-S., Stankova, B. and Zak, A. (2011). Fatty acids as biocompounds: their role in human metabolism, health and disease–a review. Part 1: classification, dietary sources and biological functions. *Biomed. Pap. Med. Fac. Univ. Palacky Olomouc Czech Repub.* **155**, 117-130. doi:10.5507/bp.2011.038
Walther, T. C. and Farese, R. V. (2012). Lipid droplets and cellular lipid metabolism. *Annu. Rev. Biochem.* **81**, 687-714. doi:10.1146/annurev-biochem-061009-102430
Wang, M. C., Min, W., Freudiger, C. W., Ruvkun, G. and Xie, X. S. (2011). RNAi screening for fat regulatory genes with SRS microscopy. *Nat. Methods* **8**, 135-138. doi:10.1038/nmeth.1556
Wang, P., Li, J., Wang, P., Hu, C. R., Zhang, D., Sturek, M. and Cheng, J. X. (2013). Label-free quantitative imaging of cholesterol in intact tissues by hyperspectral stimulated Raman scattering microscopy. *Angew. Chemie - Int. Ed.* **52**, 13042-13046.
Wang, H., Becuwe, M., Housden, B. E., Chitraju, C., Porras, A. J., Graham, M. M., Liu, X. N., Thiam, A. R., Savage, D. B., Agarwal, A. K. et al. (2016). Seipin is required for converting nascent to mature lipid droplets. *eLife* **5**, e16582. doi:10.7554/eLife.16582
Wei, M., Shi, L., Shen, Y., Zhao, Z., Guzman, A., Kaufman, L. J., Wei, L. and Min, W. (2019). Volumetric chemical imaging by clearing-enhanced stimulated Raman scattering microscopy. *Proc. Natl. Acad. Sci. USA* **116**, 6608-6617. doi:10.1073/pnas.1813044116
Welte, M. A. (2009). Fat on the move: intracellular motion of lipid droplets. *Biochem. Soc. Trans.* **37**, 991-996. doi:10.1042/BST0370991
Woodbury, E. J. and Ng, W. K. (1962). Ruby laser operation in near IR. *Proc. Inst. Radio Eng.* **50**, 2367.
Yu, Y., Ramachandran, P. V. and Wang, M. C. (2014). Shedding new light on lipid functions with CARS and SRS microscopy. *Biochim. Biophys. Acta (BBA) Mol. Cell Biol. Lipids* **1841**, 1120-1129. doi:10.1016/j.bbalip.2014.02.003
Yu, Y., Mutlu, A. S., Liu, H. and Wang, M. C. (2017). High-throughput screens using photo-highlighting discover BMP signaling in mitochondrial lipid oxidation. *Nat. Commun.* **8**, 865. doi:10.1038/s41467-017-00944-3
Yue, S., Li, J., Lee, S.-Y., Lee, H. J., Shao, T., Song, B., Cheng, L., Masterson, T. A., Liu, X., Ratliff, T. L. et al. (2014). Cholesteryl ester accumulation induced by PTEN loss and PI3K/AKT activation underlies human prostate cancer aggressiveness. *Cell Metab.* **19**, 393-406. doi:10.1016/j.cmet.2014.01.019
Zhang, C. and Cheng, J.-X. (2018). Perspective: coherent Raman scattering microscopy, the future is bright. *APL Photonics* **3**, 090901. doi:10.1063/1.5040101
Zhang, C. and Liu, P. (2019). The new face of the lipid droplet: lipid droplet proteins. *Proteomics* **19**, 1700223. doi:10.1002/pmic.201700223
Zhang, C., Huang, K.-C., Rajwa, B., Li, J., Yang, S., Lin, H., Liao, C.-S., Eakins, G., Kuang, S., Patsekin, V. et al. (2017a). Stimulated Raman scattering flow cytometry for label-free single-particle analysis. *Optica* **4**, 103. doi:10.1364/OPTICA.4.000103
Zhang, C., Li, J., Lan, L. and Cheng, J.-X. (2017b). Quantification of lipid metabolism in living cells through the dynamics of lipid droplets measured by stimulated Raman scattering imaging. *Anal. Chem.* **89**, 4502-4507. doi:10.1021/acs.analchem.6b04699
Zhang, J., Zhao, J., Lin, H., Tan, Y. and Cheng, J.-X. (2020). High-Speed Chemical Imaging by Dense-Net Learning of Femtosecond Stimulated Raman Scattering. *J. Phys. Chem. Lett.* **11**, 8573-8578. doi:10.1021/acs.jpclett.0c01598
Zumbusch, A., Holtom, G. R. and Xie, X. S. (1999). Three-dimensional vibrational imaging by coherent anti-stokes raman scattering. *Phys. Rev. Lett.* **82**, 4142-4145. doi:10.1103/PhysRevLett.82.4142
Zumbusch, A., Langbein, W. and Borri, P. (2013). Nonlinear vibrational microscopy applied to lipid biology. *Prog. Lipid Res.* **52**, 615-632. doi:10.1016/j.plipres.2013.07.003

Journal of Cell Science (2022) 135, jcs252353. doi:10.1242/jcs.252353

Journal of Cell Science